Characterization of two fast-turnaround dry dilution refrigerators for scanning probe microscopy

Mark E. Barber[1,2,3,4*], Yifan Li[1,3,4], Jared Gibson[5,6],
Jiachen Yu[1,2,4], Zhanzhi Jiang[5,6], Yuwen Hu[1,3,4], Zhurun Ji[2,3,4],
Nabhanila Nandi[1,3,4], Jesse C. Hoke[1,3,4],
Logan Bishop-Van Horn[1,3,4], Gilbert R. Arias[5,6],
Dale J. Van Harlingen[5,6], Kathryn A. Moler[1,2,3,4],
Zhi-Xun Shen[1,2,3,4], Angela Kou[5,6], Benjamin E. Feldman[1,3,4*]

[1]Stanford Institute for Materials and Energy Sciences, SLAC National Accelerator Laboratory, Menlo Park, 94025, CA, USA.
[2]Department of Applied Physics, Stanford University, Stanford, 94305, CA, USA.
[3]Department of Physics, Stanford University, Stanford, 94305, CA, USA.
[4]Geballe Laboratory of Advanced Materials, Stanford University, Stanford, 94305, CA, USA.
[5]Department of Physics, University of Illinois at Urbana-Champaign, Urbana, 61801, IL, USA.
[6]Materials Research Laboratory, University of Illinois at Urbana-Champaign, Urbana, 61801, IL, USA.

*Corresponding author(s). E-mail(s): mebarber@stanford.edu; bef@stanford.edu;

Abstract

Low-temperature scanning probe microscopes (SPMs) are critical for the study of quantum materials and quantum information science. Due to the rising costs of helium, cryogen-free cryostats have become increasingly desirable. However, they typically suffer from comparatively worse vibrations than cryogen-based systems, necessitating the understanding and mitigation of vibrations for SPM applications. Here we demonstrate the construction of two cryogen-free dilution refrigerator SPMs with minimal modifications to the factory default and we systematically characterize their vibrational performance. We measure the absolute vibrations at the microscope stage with geophones, and use both microwave

1

impedance microscopy and a scanning single electron transistor to independently measure tip-sample vibrations. Additionally, we implement customized filtering and thermal anchoring schemes, and characterize the cooling power at the scanning stage and the tip electron temperature. This work serves as a reference to researchers interested in cryogen-free SPMs, as such characterization is not standardized in the literature or available from manufacturers.

1 Introduction

The invention of the ^{3}He/^{4}He dilution refrigerator (DR) marked a pivotal milestone for experiments at ultra-low temperatures. By utilizing the enthalpy of mixing in the transition from a ^{3}He-concentrated phase to a ^{3}He-dilute phase, DRs achieve continuous refrigeration down to the milli-Kelvin regime. Since the pioneering work of Das et al. in 1965 [1], which achieved a temperature of 0.22 K, subsequent design improvements have facilitated base temperatures below 10 mK [2], pushing the boundaries of accessible temperatures for scientific exploration, and making DRs indispensable tools in modern quantum materials and quantum information research.

The operation of DRs relies on a stable pre-cooling environment in the Kelvin regime to liquefy the helium mixture and maintain ^{3}He circulation. For cryogen-based ("wet") DRs, the pre-cooling environment is achieved by immersing the system in a liquid ^{4}He bath at ∼4 K and pumping on a small volume of the ^{4}He, known as a 1 K pot. In wet systems, the liquid ^{4}He bath typically boils off over days-long timescales, requiring the users to regularly refill the helium. Additionally, due to global helium shortages and increasing costs of liquid helium, the operation of wet DRs has become increasingly unappealing. An alternative route to achieve low temperatures is to use cryogen-free ("dry") DRs, where a closed-cycle pulse tube refrigerator pre-cools the cryostat to ∼4 K and a Joule–Thomson stage condenses the circulating ^{3}He. This alleviates the need for a liquid helium supply, but at the cost of increased mechanical vibrations from the pulse tube [3–6]. These vibrations make dry DRs a challenging platform for scanning probe experiments, where ultra-low vibrations are essential.

The conventional wisdom for achieving a low vibration scanning probe microscope (SPM) is to make the microscope structure as stiff as possible and isolate it from vibration sources using a damped spring stage, such that the cut-off frequency of the spring stage precludes exciting vibrational modes of the microscope [7]. For a wet DR this can mean floating the whole cryostat on air springs to isolate it from a noisy environment, but for a dry DR where the dominant source of vibrations is the pulse tube cooler, the vibration isolation has to be internal to the DR.

One possible isolation scheme is to attach the scanning stage to a large mass and suspend it on springs below the mixing chamber [8, 9]. This method has been used for scanning gate microscopy [10] and near-field scanning microwave microscopy [11], using 6 kg and 5 kg masses respectively. By additionally suspending the whole still stage and dilution unit on springs, and using three 5 kg spring stages in series below

the mixing chamber, scanning tunneling microscopy and magnetic resonance force microscopy have been demonstrated [12]. However, these designs require heavy modification to the DR, and the spring stages severely limit the cooling power available for the microscope [10]. Furthermore, if the DR incorporates a magnet, this can limit the space available for spring extension below the mixing chamber, and the whole microscope and suspended stage must be constructed from non-magnetic components to prevent unwanted motion in applied magnetic field [10].

The combination of low temperature and high magnetic field is often advantageous for the investigation of quantum materials. This motivates an alternative route to implement the isolation between the pulse tube cooler and the DR: rigidly mounting the microscope to the mixing chamber. Many modern dry DRs have this type of isolation installed by the manufacturer, and scanning systems in such cryostats have been implemented for scanning superconducting quantum interference device (SQUID) microscopy [13] and for scanning nitrogen-vacancy magnetometry [14]. An additional benefit of this scheme is that a fast-turnaround sample loader can be used for the microscope to drastically improve sample cool-down and warm-up times from days, in a system with a magnet installed, to hours. Fast-turnaround sample loaders have been used to implement scanning SQUID-on-tip microscopy [15], and scanning microwave impedance microscopy [16].

Despite the number of demonstrated microscopes, the large variance in calibration methods and vibration isolation strategies makes it challenging to derive a definitive estimate of the expected impact a dry DR has on scanning performance based solely on this existing body of research [10, 12, 13, 15]. Therefore, systematically characterizing the vibrations of modern dry DR systems is crucial for future high resolution SPMs.

In this paper, we describe two fast-turnaround scanning probe microscopy systems implemented in commercial bottom-loading dry DRs with minimal customization to the factory-default systems. We characterize the absolute magnitude of vibrations in the bottom-loading sample pucks using geophone measurements, both with and without the pulse tube running. We show that details of the cryostat resonances and their overlap with pulse tube harmonics dictate which modes contribute most prominently to the vibrational noise. We further construct two SPMs based on stacks of commercial positioners from Attocube rigidly mounted in the sample puck. We determine the relative tip-sample vibrations at low temperatures using scanning microwave impedance microscopy (MIM) and a scanning single-electron transistor (SET), using the method of characterizing the noise spectral density in a known signal gradient [13, 15, 17–19]. Additionally, we discuss the cooling power available for the microscope and describe specially designed filtering schemes that allow us to achieve an electron temperature of <30 mK in the scanning probe, characterized by Coulomb blockade thermometry with a scanning SET. We end with a summary of the key design criteria to mitigate vibrations and a discussion of possible ways to further improve the performance of these systems.
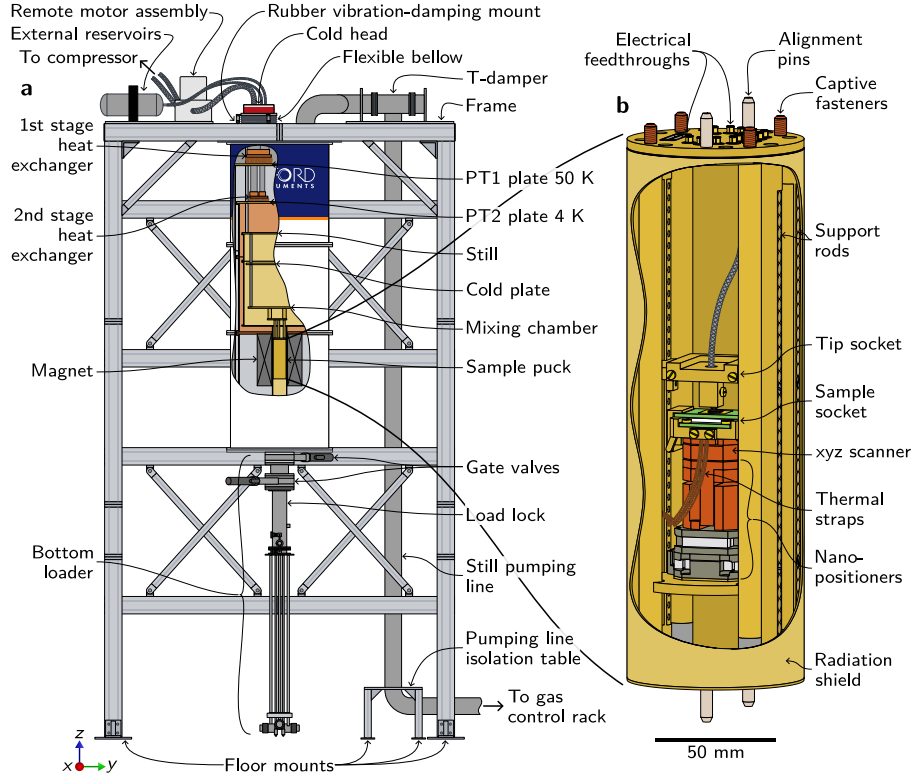
Fig. 1 **a** Schematic overview of the dilution refrigerator design including the factory installed vibration isolation measures. **b** Schematic of a bottom loading sample puck housing the scanning probe microscope for system 1. See Supplementary Information for photographs and additional details of both systems.

2 Cryostat and microscope design

Our SPMs are implemented in Oxford Instruments ProteoxMX DRs with base temperatures of 8 mK at the mixing chamber for system 1 and <10 mK for system 2. The systems incorporate superconducting vector magnets with a 6 T vertical solenoid and 1 T in-plane coils for both horizontal directions. Pre-cooling in both systems is provided by a PT415 pulse tube cryocooler from Cryomech with remote motor option, driven by a CPA1110 compressor, which provides a cooling power of 1.35 W at 4.2 K.

The pulse tube achieves cooling though the cyclic expansion of compressed helium gas. The remote motor turns a rotary valve that alternately connects the pulse tube inlet to the high and low pressure sides of the compressor, oscillating the pressure between 2 and 0.6 MPa at a frequency of 1.4 Hz. The surge of gas as the valves open and close leads to the characteristic chirping sound of a pulse tube cooler and induces mechanical vibrations as parts of the pulse tube cooler expand and contract.

Several vibration isolation measures are implemented by Oxford Instruments to limit the mechanical coupling between the pulse tube and the rest of the DR; see Fig. 1a for an overview. The cold head of the pulse tube is sealed to the outer vacuum can of the DR using a flexible vacuum bellows and the weight of the cold head is supported on

4

rubber dampers. The cold ends of the two-stage cryocooler are joined to the respective plates, PT1 and PT2, in the cryostat through soft flexible copper braids. The remote motor and external reservoirs for the two cooling stages are mounted directly on the top of the cryostat frame. The top plate of the frame weighs about 100 kg, and the frame has mounting plates for anchoring to the laboratory floor. The remote motor of the pulse tube is driven by a linear microstepping drive from Precision Motion Controls with 50,000 steps per revolution to help reduce vibrations that can come from the jerking motion of a stepper motor and to limit the electromagnetic interference created by rapid changes in current through the motor windings. The compressor for the pulse tube cooler in both systems is housed in an adjacent pump room.

Additional measures are taken to limit vibrations from operation of the DR. For system 1, the gas handling system that circulates the ^{3}He is housed in the adjacent pump room with the compressor. For system 2 it is next to the cryostat, but to prevent additional vibrations due to the pumps in the gas handling system, both systems utilize an additional isolation table for the still pumping line that can be anchored to the floor. The still pumping line also incorporates a flexible bellows type, T-damper on the top of fridge to further reduce vibrational coupling.

The cool-down time for these systems with the magnet installed is approximately 3 days due to the limited cooling power of the pulse tube cooler compared to that of liquid helium. To facilitate faster turnaround times for exchanging the sample, a bottom loading mechanism allows the sample to be exchanged without the need to warm the entire cryostat to room temperature [20]. This has the added benefit that the sample space can be accessed without having to dismantle the nested set of vacuum cans and radiation shields, and remove the magnet. The sample puck, Fig. 1b, that houses the microscope is loaded into the DR from a load lock under the system. It passes through spring loaded flaps in each of the radiation shields before being bolted on to the cold finger of the mixing chamber using four captive M5 fasteners driven by piston sealed drive rods from outside the fridge. The puck and cold finger are both gold plated to improve the thermal interface between the puck and the mixing chamber. After the puck is attached to the cold finger, the bottom loader is fully retracted from the system. This mechanism allows the microscope to be installed on the cold finger in a manner comparable to that as if the whole fridge had been fully opened to install it. After pumping the load lock, loading the sample puck can be accomplished by one person in less than 15 minutes, and the DR cools back down to base temperature automatically in about 8 hours. Active gas gap heat switches between the mixing chamber and the cryocooler are utilized for the initial cooling from room temperature to ∼6 K, before the system automatically switches back to the operation of the dilution unit to reach base temperature.

This bottom loading configuration enables efficient use of the available space and cooling power of the DR for electrical wiring and other services installed and thermally anchored in the cryostat. Each puck has two 51-way Nano-D connectors for DC wires and up to 28 SMP connectors for coaxial high frequency connections. With all our wiring installed, including low resistance DC wiring for driving up to eight nanopositioners, the measured cooling power available at the mixing chamber is 450 μW at 100 mK, and the expected cooling power in the sample puck is ∼100 μW [20].

We have designed two SPMs which are rigidly mounted to the sample puck body as a support structure. The microscope used for imaging and tip-sample vibrational characterization is described below (see Supplementary Information for a detailed description of the second microscope and photographs of both). The puck has four vertical support rods with through holes for bolts, so we attached two horizontal plates across the puck, one to hold a stack of nanopositioners and the sample, and the other to hold the tip (Fig. 1b). The plates can be positioned in increments of 2.5 mm, so the microscope can accommodate different probe lengths and sample heights while ensuring the tip and sample always meet at the center of the vector magnetic field. For nanopositioners, we use inertia-based positioners from Attocube for coarse positioning, models ANPx311/RES+/LT/HV and ANPz102/ULT/RES+/HV, and flexure-based model ANSxyz100/CuBe/LT/HV for fine scanning. The sample socket is made from gold plated oxygen-free high thermal conductivity (OFHC) copper and clamps a removable PCB to which the sample is mounted. A calibrated ruthenium-oxide temperature sensor is mounted to the sample socket, and the thermal connection to the cold body of the puck is provided by two clamped OFHC copper braids, each $\sim$10 cm long with 320 strands of 70 μm wire each, as a compromise between flexibility and thermal conductivity.

3 Vibration characterization

To understand the vibrational characteristics of each system, we first measure the absolute vibrations of the sample pucks where the microscopes will be housed, see Sec. 3.1 below. To assess the impact of the vibrations on the scanning performance, we then turn to directly characterizing the relative tip-sample displacement in the microscope of system 1 using MIM and SET measurements as detailed in Sec. 3.2.

3.1 Absolute vibrations of the sample puck

To measure the absolute vibrations of the sample puck while installed in the DR, we use geophones mounted in the puck at the position where the nanopositioners would normally be installed, see Fig. 1b. We use models GS-11D and GS-ONE LF from Geospace Technologies that both have resonance frequencies of 4.5 Hz at room temperature, and are compact enough to fit inside the sample puck. Below this resonance frequency, the geophone sensitivity decreases quickly, setting an effective lower limit for detecting vibrations of about 1 Hz. In three separate cool-downs, we respectively measure a vertical geophone and a horizontal geophone oriented along the x and y directions indicated in Fig. 1, calibrating the geophone at low temperatures for each measurement [21].

We first detail the measurements from system 1. The amplitude spectral density (ASD) of the sample puck displacement is plotted in Fig. 2a,b, comparing the performance with the pulse tube cooler running and with it turned off while the DR is at a temperature of 5 K. We define the total integrated root-mean-square (RMS) vibration
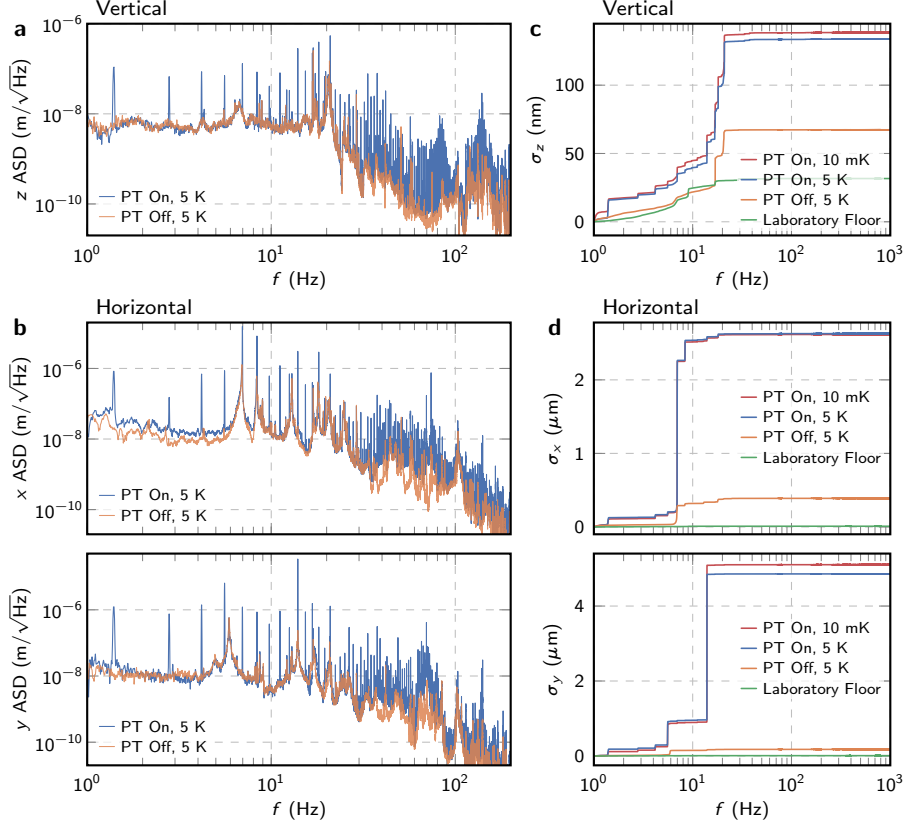
Fig. 2 a Amplitude spectral density (ASD) of vibrations measured in the vertical direction of the sample puck mounted in the dilution fridge, with the pulse tube (PT) cooler on and off at a temperature of 5 K. Measurements are from system 1. **b** Vibration measurements for the horizontal directions, x and y, as defined in Fig. 1. **c–d** Cumulatively integrated root mean square (RMS) vibration amplitude in the vertical direction σ_z (**c**) and the horizontal directions σ_x and σ_y (**d**).

amplitude, σ_{u_i}, between two frequencies f_1 and f_2 as

$$\sigma_{u_i}(f_1, f_2) = \sqrt{\int_{f_1}^{f_2} [\delta u_i]^2 \, \mathrm{d}f},\tag{1}$$

where δu_i is the ASD of displacement in the $u_i = x$, y, or z direction. In Fig. 2c,d we show the cumulatively integrated vibration from 1 Hz to 1 kHz for the cases with the pulse tube on and off at 5 K. We also provide comparison curves with the DR running at 10 mK, and the ambient vibration amplitude measured on the laboratory floor directly under the DR with the pulse tube off.

The effect of the pulse tube cooler can be clearly seen in the vibration spectra, Fig. 2a,b, appearing as a frequency comb of harmonics of the pulse tube frequency, 1.4 Hz, all the way up to the highest measured frequencies. However, the spectral weight of most of these peaks is relatively small, as can be seen in Fig. 2c,d. In the

7

horizontal directions the spectral density peak from the pulse tube at 1.4 Hz is around $1\,\mu\mathrm{m}/\sqrt{\mathrm{Hz}}$ and the integrated amplitude is $\sim$100 nm. At frequencies higher than 20 Hz, the integrated amplitude of each pulse tube harmonic is generally below $\sim$20 nm. In the vertical direction, the overall amplitudes are an order of magnitude smaller.

The dominant contributions to the total integrated amplitude appear to come from structural modes of the cryostat that are close in frequency to a harmonic of the pulse tube frequency and are therefore excited more strongly while the pulse tube is running. These can be identified by comparing the vibration spectra with the pulse tube on and off. The dominant contribution is at 7 Hz for the x direction and 14 Hz for the y direction. In contrast, the structural mode at $\sim$5.9 Hz in the y direction does not coincide with a harmonic of 1.4 Hz, and it is not more strongly excited with the pulse tube on. However, the nearest harmonic at 5.6 Hz contributes more strongly than its neighboring harmonics. Running the dilution unit does not significantly increase the total vibration amplitude; the pulse tube cooler still remains the dominant source of vibrations (Fig. 2c,d).

In the vertical direction, the total integrated RMS vibration up to 1 kHz is 140 nm. In the horizontal directions, it is 2.6 μm along x and 5.1 μm along y. All the dominant vibrations are below $\sim$20 Hz. Comparing to a system with the same model of pulse tube cooler, but that uses a rigid bolted connection rather than flexible copper braids between the pulse tube and the DR, the influence of the pulse tube is significantly reduced, particularly for z motion [10]. Specifically, Pelliccione et al. [10] observed an integrated vertical vibration amplitude of 1.9 μm at the mixing chamber of their DR and 0.6 μm on their decoupled spring stage. Horizontally, they observed $\sim$6 μm in both directions on the mixing chamber which was reduced to $\sim$1.5 μm on the spring stage, but in their work most of the remaining vibrations were at low frequencies below 10 Hz. The flexible mount and copper braid thermalization scheme for the pulse tube in our DR is therefore helpful to minimize the vibrations in the environment of the microscope.

To provide a second point of comparison, we conduct analogous characterization of the vibrations in the sample puck of system 2, see Supplementary Information for plots of the full vibration spectra. In system 2, the total integrated RMS vibration amplitude from 1–200 Hz is similar in all three directions to that of system 1, although the vibration peaks are distinct. Comparing the two systems highlights the importance of the precise frequencies of structural modes, and measurements from system 2 before and after the vibration damping mounts of the cold head were correctly configured highlight the importance of the exact pulse tube mounting.

As an illustrative example, in Fig. 3 we show a detailed comparison of the y vibration spectrum between 4 Hz and 16 Hz for the two systems, both with the pulse tubes running and with them turned off. The primary structural modes in this frequency range for system 1 occur at 5.9 Hz and 14 Hz (arrows in Fig. 3a), as previously identified. In the preliminary testing of system 2, the presumably equivalent modes were both at slightly lower frequencies, 5.6 Hz and 13.5 Hz (arrows in Fig. 3c). A substantially larger contribution at the 1.4 Hz pulse tube frequency was initially observed for system 2, see Supplementary Information, however, on further inspection of the system, it was identified that the isolation of the pulse tube from the cryostat was not

Fig. 3 a A replication of the amplitude spectral density (ASD) of vibrations measured in the y direction in the sample puck of system 1 from Fig. 2, but on a finer scale from 4 Hz and 16 Hz, showing data with the pulse tube (PT) cooler on and off, at a temperature of 5 K. Vertical lines mark harmonics of the 1.4 Hz pulse tube frequency. Two identified structural modes of the cryostat are indicated by arrows. **b** Cumulatively integrated (starting from 4 Hz) vibration power spectral density (PSD). **c–d** Analogous vibration spectra measured in system 2 while the room temperature mounting flange of the pulse tube cold head is rigidly connected to the top plate of the cryostat showing the vibration ASD (**c**) and integrated PSD (**d**). Arrows indicate the shifted structural modes. **e–f** The vibration spectra of system 2 when the cold head is supported by rubber vibration damping legs showing the vibration ASD (**e**) and integrated PSD (**f**).
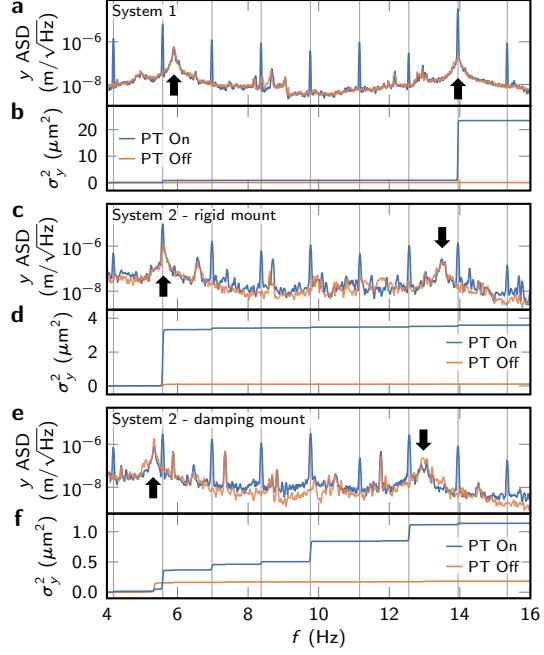
correctly implemented during installation. The room temperature mounting flange of the cold head was rigidly connected to the top plate of the cryostat rather than sitting on its rubber vibration damping legs. After correcting the installation the 1.4 Hz peak was reduced and the two identified structural modes also shift to slightly lower frequencies (arrows in Fig. 3e). The observed differences between the two systems likely reflect slight differences in their design. For example, system 1 is 275 mm taller to accommodate a double gate valve on the bottom loader, which allows samples to be transferred from a glove box to the DR without exposing them to air. In addition, the remote motor and high pressure lines are oriented in different directions in each system, and system 2 is not bolted to the floor.

To compare the spectral weight between different frequencies, we plot the integrated power spectral density. For system 1, plotted in Fig. 3b, the 14 Hz mode results in the largest vibration when the pulse tube is turned on. This is because it coincides with a harmonic of the pulse tube. However, for the initial configuration of system 2 with the cold head rigidly connected, the corresponding mode at 13.5 Hz is not resonant with a pulse tube harmonic, and it has a smaller contribution to vibrations when the pulse tube is running (Fig. 3d). The situation is reversed for the lower frequency mode: the 5.6 Hz mode of system 2 initially matched a pulse tube harmonic and had a larger contribution with the pulse tube on. In the final configuration of system 2 with the cold head supported by rubber legs, neither mode is resonant with a pulse tube harmonic and the overall contribution from this frequency range is much smaller (Fig. 3f). These differences emphasize the importance of considering details of the structural modes of the cryostat and optimizing design to minimize overlap between the structural modes and the pulse tube harmonics.

3.2 Relative tip-sample vibrations

We now turn to direct measurements of the relative tip-sample vibrations in the SPM. This is the important figure of merit for a scanning probe system, as it characterizes the scanning performance in the configuration used for experiments. If the microscope is stiff enough, it can act as a 'high-pass' filter and low frequency vibrations will cause the tip and sample to move together without hindering scanning performance. If, however, there are softer modes that overlap with the absolute vibrations of the sample puck discussed above, relative tip-sample motion can be excited.

We first describe MIM measurements of the relative tip-sample vibrations of the microscope mounted in system 1 characterized above. MIM measures the admittance between a sharp tip and the sample at microwave frequencies and is sensitive to changes of local conductivity and permittivity with nanoscale spatial resolution; see recent reviews [22] and [23] for more details. Figure 4a shows the sharp metallic tip approached close to a sample, a gold film deposited on a Si/SiO_2 substrate, and a simplified schematic of the readout scheme for the MIM signal. The imaginary part of the MIM signal, MIM-Im, characterizes the screening of the tip's electric field by the sample, and it diverges as the tip approaches a metallic sample. This can be used as a sensitive measure of the tip-sample vibrations in the z-direction since any vibrations will appear as additional noise in the MIM signal, and the frequency dependence of the noise will contain information about the vibration spectrum. By positioning above a spatially uniform region of the gold film, such that there is little signal change with lateral motion of the tip, the z vibration spectrum can be independently obtained. The total noise δMIM-Im can be decomposed as

$$\delta\text{MIM-Im}^2 = \delta\text{MIM-Im}_{\text{intrinsic}}^2 + \left(\delta z_{\text{t-s}}\frac{\partial\text{MIM-Im}}{\partial z_{\text{t-s}}}\right)^2, \tag{2}$$

where the intrinsic MIM noise δMIM-Im$_{\text{intrinsic}}$ is assumed to add independently, in quadrature, with the tip-sample vibrational noise, $\delta z_{\text{t-s}}$, and we assume the MIM-Im signal changes linearly with distance on the scale of the vibrations.

Figure 4c shows the ASD of the MIM-Im noise signal with the tip positioned $\sim$2 μm above the sample, where the MIM signal is approximately linear over a few hundred nanometers in z (Fig. 4b), and the measured intrinsic MIM noise floor at a temperature of 10 mK. The intrinsic MIM noise is mostly limited by the output noise of the first amplification stage, which for our measurement is a cryogenic low noise amplifier mounted to the 4 K stage of the DR. We measure this intrinsic noise by disconnecting the excitation to the MIM tip and instead directly drive the input of the amplifier through a second directional coupler normally used for nulling the MIM signal at a particular position. The total noise is dominated by vibrations at most frequencies. Subtracting the power spectral densities and integrating, we obtain the integrated RMS vertical tip-sample vibration amplitude $\sigma_{z_{\text{t-s}}}$, plotted in Fig. 4d. The total integrated vibration up to 1 kHz is 29 nm. The dominant vibrations are in the range 100–300 Hz, with the largest peaks at 114 Hz (contributing 7 nm amplitude), 122 Hz (10 nm), $\sim$200 Hz (22 nm), and 312 Hz (7 nm). These are likely structural modes of the microscope body or nanopositioners that are being excited by the residual
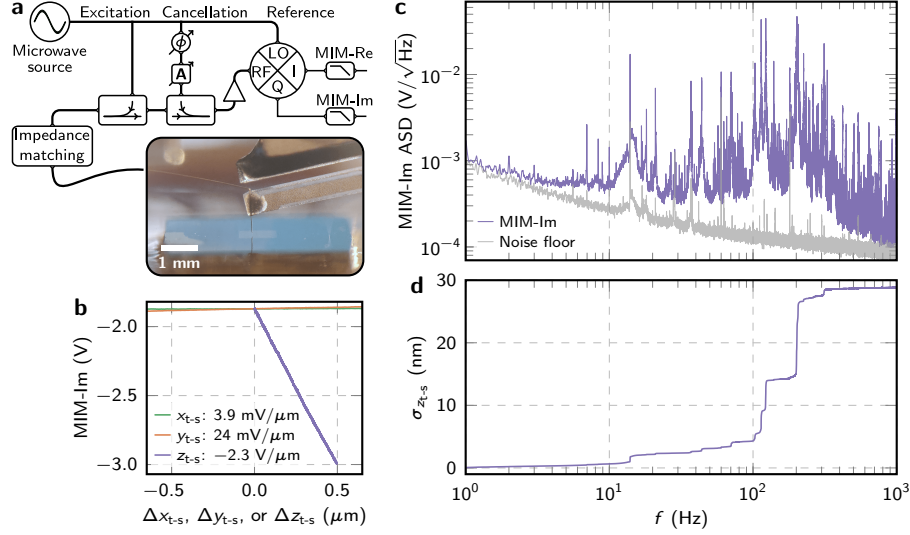
Fig. 4 **a** Image of the microwave impedance microscopy (MIM) tip affixed to a tuning fork, positioned above a sample, and a schematic of the MIM readout circuit [23, 24]. **b** Change in MIM signal MIM-Im with relative tip-sample position and linear fitting results along all three cartesian axes, at a height of 2 μm above a metallic film. **c** Amplitude spectral density (ASD) of the MIM noise measured at the same location as **b**, and a measurement of the MIM noise floor, see text for details. **d** Integrated tip-sample RMS vibration amplitude in the z direction, $\sigma_{z_{\text{t-s}}}$.

motion of the puck at these higher frequencies. Many harmonics of the fundamental pulse tube frequency are visible in the vibration spectrum, but the spectral weight of most are small compared to the vibrations identified above.

The relative xy vibrations between the tip and sample can be measured when the in-plane gradient of the signal is comparable to the z gradient. However, at this level of z vibration, the response in z remains the dominate source in the overall noise, such that we cannot reliably extract xy vibrations. To obtain a second independent measure of vertical tip-sample vibrations and address the xy vibrations in our system, we use a different probe: a scanning SET [25].

The scanning SET tip used in this work (Fig. 5a) consists of source and drain electrodes separated from a metallic island by tunnel junctions, all evaporated on a pulled quartz rod as described in Ref. [26]. The small size of the island, $\sim$100 nm in diameter, leads to a large charging energy $E_{\text{c}} \sim 1$ meV due to the large Coulomb repulsion from electrons already on the island. Therefore, when the temperature is much lower than E_{c}, current can only flow through the SET when the energy of a state in the island matches the Fermi level of the leads [27]. The former depends on the electrostatic environment, giving rise to a sensitive response of SET current I_{SET} to the local electrostatic potential.

To measure the relative tip-sample vibrations with the SET, we bring it close to a gold film with patterned holes deposited on a grounded Si/SiO$_2$ wafer. This serves as a test sample and we apply a voltage V_{g} to the film to electrostatically gate the SET. The applied potential difference and the different work functions of the film, substrate

11
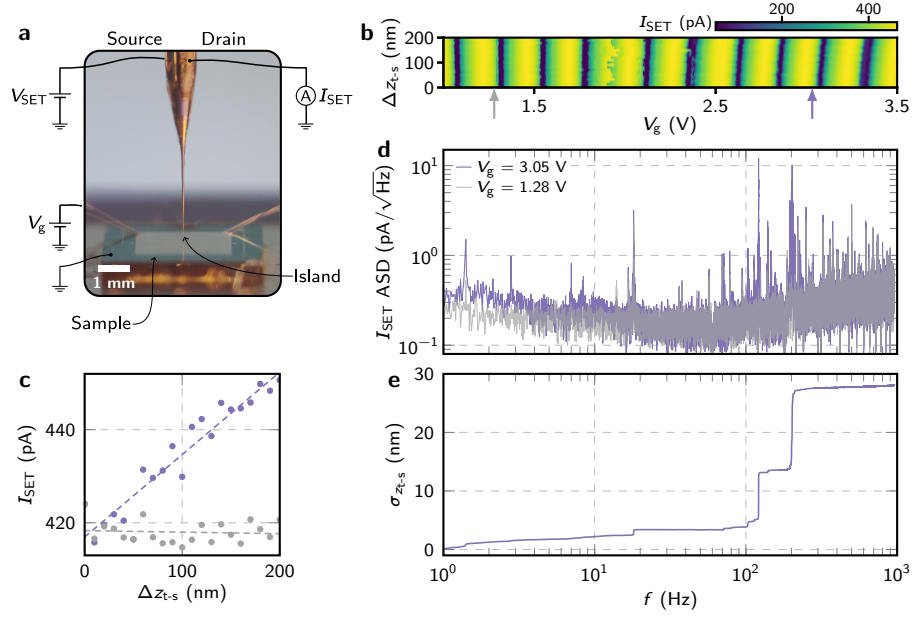
Fig. 5 **a** Image of the scanning single-electron transistor (SET) above a sample, with the schematic measurement circuit overlaid and SET components labeled. **b** Current through the SET I_{SET} as a function of gate voltage V_{g} and change in tip-sample distance $\Delta z_{\text{t-s}}$ (note that $\Delta z_{\text{t-s}} = 0$ does not correspond to zero tip-sample distance). The applied SET source-drain bias is $V_{\mathrm{SET}} = 2.75$ mV. **c** I_{SET} as a function of $\Delta z_{\text{t-s}}$ at two different gate voltages. At $V_{\mathrm{g}} = 1.28$ V, I_{SET} is independent of $z_{\text{t-s}}$, whereas it varies linearly with $z_{\text{t-s}}$ at $V_{\mathrm{g}} = 3.05$ V. **d** Amplitude spectra density (ASD) of the filtered I_{SET} at the two V_{g} values in **c**, see text for details of the filtering. **e** Integrated tip-sample RMS vibration amplitude in the z direction, $\sigma_{z_{\text{t-s}}}$, from SET measurements.

and tip, lead to spatial gradients in the electrostatic potential along the x, y, and z directions, which affect the measured I_{SET} as the tip moves relative to the sample. In general, assuming I_{SET} varies linearly as a function of spatial position, at any given frequency f, the tip-sample vibrations couple into the current noise as

$$\delta I_{\mathrm{SET}}^2(f) = \delta I_{\mathrm{SET},0}^2(f) + \left[\nabla_{\text{t-s}} I_{\mathrm{SET}} \cdot \delta \boldsymbol{r}_{\text{t-s}}(f)\right]^2, \tag{3}$$

where δI_{SET} denotes the total SET current noise amplitude spectral density, $\delta I_{\mathrm{SET},0}$ is assumed to be uncorrelated noise that does not arise from tip-sample vibrations, such as electronic noise, $\nabla_{\text{t-s}} = \frac{\partial}{\partial x_{\text{t-s}}}\boldsymbol{e_x} + \frac{\partial}{\partial y_{\text{t-s}}}\boldsymbol{e_y} + \frac{\partial}{\partial z_{\text{t-s}}}\boldsymbol{e_z}$ is the gradient operator, and $\delta \boldsymbol{r}_{\text{t-s}} = \delta x \boldsymbol{e_x} + \delta y \boldsymbol{e_y} + \delta z \boldsymbol{e_z}$ is the displacement vector of tip-sample vibrations.

We first describe measurements of vibrational noise along the z direction that corroborate the MIM result. To exclude contributions from lateral vibrations, we perform our measurements above a uniform region of the gold film, where in-plane gradients are minimal, and Eq. 3 thus reduces to

$$\delta I_{\mathrm{SET}}^2 = \delta I_{\mathrm{SET},0}^2 + \left(\delta z_{\text{t-s}} \frac{\partial I_{\mathrm{SET}}}{\partial z_{\text{t-s}}}\right)^2. \tag{4}$$

12

In Fig. 5b, we plot I_{SET} as a function of V_g as we vary the height of the tip at an approximate tip-sample distance of ~ 1 μm. We observe that the period of the Coulomb blockade oscillations decreases as the tip approaches the sample due to the increased tip-sample capacitance [27]. The corresponding change in I_{SET} as a function of $\Delta z_{t\text{-}s}$ can then be utilized to measure $\delta z_{t\text{-}s}$ by comparing the current noise spectra at two distinct gate voltages with different gradients.

We first measure the SET current noise at $V_g = 3.05$ V (purple arrow in Fig. 5b). At this gate voltage, $I_{SET} \sim 420$ pA and it has a linear dependence on $\Delta z_{t\text{-}s}$ (Fig. 5c). Another current noise spectrum is taken at $V_g = 1.28$ V (gray arrow in Fig. 5b), which maintains the same current set point to keep non-vibrational noise contributions of the SET consistent between each measurement, but has minimal z gradient. Near this voltage, the work function difference between the tip and the sample is compensated so that the sample no longer gates the SET. It therefore realizes a condition, termed 'flat band' in the SET literature, where I_{SET} is independent of $z_{t\text{-}s}$ (Fig. 5c) and the SET current noise should only consist of non-vibrational contributions.

We note that in our measurement, a significant portion of the total noise spectral weight comes from non-vibrational noise, which exhibits small variations between measurements. To prevent artifacts from the non-vibrational component in Eq. 3, we therefore apply a series of digital notch filters to remove the non-vibrational noise at identified frequencies (see Supplementary Information for detailed discussions). Serendipitously, the frequencies at which the non-vibrational noise dominates do not coincide with prominent vibrational noise peaks, enabling them to be reliably separated. We show the filtered ASD spectra for current noise in Fig. 5d. Noise at the characteristic frequency of the pulse tube and its harmonics can be seen in the data, but, like the MIM measurements, its spectral weight is small. Subtracting the power spectral densities and integrating, we obtain $\sigma_{z_{t\text{-}s}}$ as measured by the SET, plotted in Fig. 5e. The total integrated RMS relative tip-sample z-vibration, slightly less than 30 nm, is consistent across measurements at different V_g (see Supplementary Information) as well as with the result from the MIM measurements. The largest contributions also occur at similar frequencies in the 100–300 Hz range. This supports our hypothesis that these vibrations are likely associated with modes of the microscope/nanopositioners rather than the specific scanned probe.

An analogous method can be used to determine in-plane tip-sample vibrations by measuring near the lithographically defined holes in the gold film. The work function mismatch between the gold film and the Si/SiO$_2$ substrate, in combination with the V_g applied to the gold film, result in an electrostatic potential gradient near the edges of the holes. When the SET is brought close to these edges, the electrostatic potential gradient induces strong in-plane spatial modulation of I_{SET}, as illustrated by the constant-height $I_{SET}(x, y)$ map taken near one corner of a patterned hole in Fig. 6a. Curves with constant I_{SET} in the image can be interpreted as equipotential contours at the height of the probe.

To illustrate the xy vibration measurement procedure we focus on two spatial locations, marked by the blue and red crosses in Fig. 6a. The I_{SET} measured along two linear trajectories through each of these points in the x and y directions (Fig. 6b) shows a strong anisotropic response for the two locations: the blue (red) location has

13
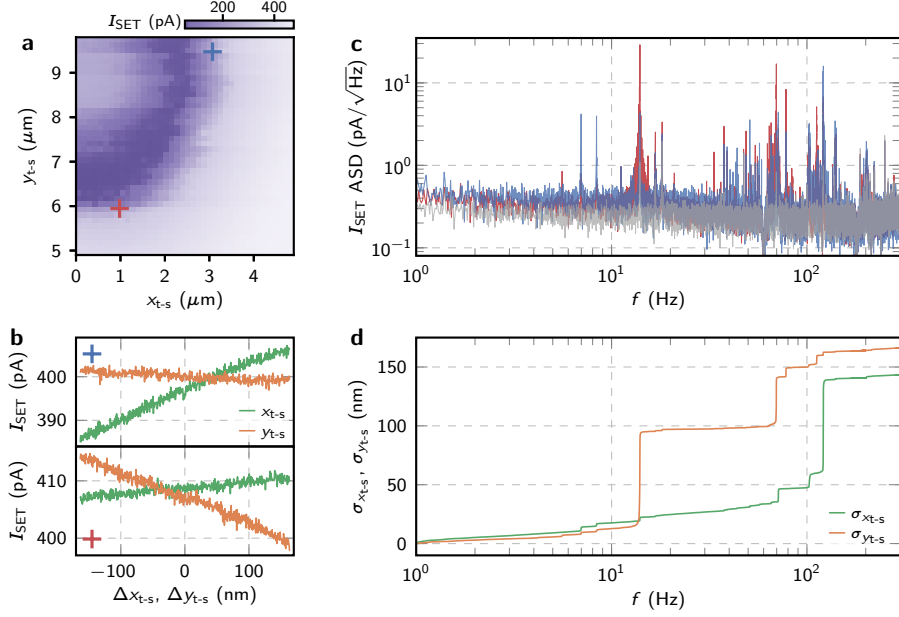
Fig. 6 **a** Map of $I_{\mathrm{SET}}(x,y)$ near a patterned hole in the gold film on the test sample. The gradient is dominated by large $\partial_x I_{\mathrm{SET}}$ ($\partial_y I_{\mathrm{SET}}$) at the location marked by a blue (red) cross. **b** The dependence of I_{SET} (at the flat band gate voltage) along the x (green) and y (orange) directions relative to the blue cross (upper panel) and the red cross (lower panel) in **a**. **c** Filtered amplitude spectral density ASD (see text) of I_{SET} taken near the flat band gate voltage at $I_{\mathrm{SET}} \sim 400$ pA. The blue (red) curve is measured at the blue (red) cross in **a** and dominated by the vibrational noise along the x (y) direction. The gray trace is measured far from the hole in the film and only includes contributions from non-vibrational noise. **d** Integrated RMS tip-sample vibrations $\sigma_{x_{\mathrm{t\text{-}s}}}$ and $\sigma_{y_{\mathrm{t\text{-}s}}}$ along the x and y directions (green, orange) fitted from vibration measurements at multiple spatial locations (see Supplementary Information).

large $\partial I_{\mathrm{SET}}/\partial x$ ($\partial I_{\mathrm{SET}}/\partial y$), but small $\partial I_{\mathrm{SET}}/\partial y$ ($\partial I_{\mathrm{SET}}/\partial x$). We measure I_{SET} noise spectra at these two locations near the local flat band voltage, to minimize z-vibration contributions while ensuring the same $I_{\mathrm{SET}} \sim 400$ pA setpoint. The corresponding I_{SET} ASD (again filtered to remove non-vibrational noise, see Supplementary Information) at these locations is shown in Fig. 6c along with a measurement further away from the feature with minimal vibrational contribution.

In principle, these current noise spectra can be converted to in-plane vibrational noise using the measured gradients. However, even though the above spectra provide a good facsimile for vibrational noise along one specific cardinal direction, perfect decoupling is challenging and in general, vibrations in both directions may contribute to the measured noise at a given location. Therefore, we measure similar spectra at multiple spatial locations (see Supplementary Information Fig. S8). Each of these locations exhibits different spatial gradients along each direction. A correlation analysis shows that the major in-plane vibrational peaks only correlate to either one of the in-plane cardinal directions (see Supplementary Information), which leads to a further

simplification of Eq. 3 when x and y vibrations are decoupled from each other:

$$\delta I_{\mathrm{SET}}^2 = \delta I_{\mathrm{SET},0}^2 + \left(\delta x_{\mathrm{t\text{-}s}}\frac{\partial I_{\mathrm{SET}}}{\partial x_{\mathrm{t\text{-}s}}}\right)^2 + \left(\delta y_{\mathrm{t\text{-}s}}\frac{\partial I_{\mathrm{SET}}}{\partial y_{\mathrm{t\text{-}s}}}\right)^2. \qquad (5)$$

We therefore fit the filtered I_{SET} power spectral density with respect to squared gradients $(\partial I_{\mathrm{SET}}/\partial x)^2$ and $(\partial I_{\mathrm{SET}}/\partial y)^2$ at every frequency. The fitted coefficients, as functions of frequency, correspond to $\delta x_{\mathrm{t\text{-}s}}^2$ and $\delta y_{\mathrm{t\text{-}s}}^2$ (see Eq. 5). The cumulatively integrated RMS x- and y-vibration amplitudes are plotted as functions of frequency f in Fig. 6d. The integrated RMS vibration amplitudes from 1 Hz to 300 Hz, $\sigma_{x_{\mathrm{t\text{-}s}}}$ and $\sigma_{y_{\mathrm{t\text{-}s}}}$, are about 140 nm and 170 nm, respectively. These in-plane vibrations are significantly larger than the out-of-plane vibration amplitude $\sigma_{z_{\mathrm{t\text{-}s}}}$, similar to the findings from geophone measurements. Comparing with the absolute vibration of the sample puck measured by the geophones, there is some direct coupling to the tip-sample vibrations. In the x direction the largest vibrations identified with the geophone, ~ 7 Hz and ~ 8.4 Hz, have a small contribution to the relative tip-sample vibration. In y, however, where the largest absolute vibration at ~ 14 Hz was observed, there is a significant contribution to the tip-sample vibration. The remainder of the dominant tip-sample vibrations are at higher frequencies, similar to the z direction, and these are likely structural modes of the microscope body or nanopositioners.

4 Temperature characterization

The available cooling power in the sample puck is lower than that at the mixing chamber, and it is important to determine the temperature that can be obtained for the sample and probe while the microscope is in operation, as well as characterize the corresponding electron temperature. We carry out this characterization in the microscope of system 1. In our microscope the sample is fixed on the nanopositioner stack, and as a consequence has a relatively weaker thermal coupling to the sample puck. This needs to be taken into consideration to account for sources of heat at the sample stage, such as Joule heating due to large contact resistances of certain samples, and the additional heat load from the operation of the piezoelectric-based scanner. The construction of the nanopositioners does not provide a strong thermal connection through the stack, so the sample socket is thermalized by two OFHC copper braids that are flexible enough so that they do not hinder the motion of the nanopositioners. One end of each copper braid is clamped to one of the gold plated support rods of the puck with a sandwiching block and two screws, and the other end is clamped to the gold plated sample socket, see Fig. 1b. Our microscope also utilizes two bearing-based coarse positioners for the x and y motion for increased rigidity, but these are made from titanium that becomes superconducting below ~ 400 mK at zero magnetic field, additionally hindering the thermal anchoring. We characterize this configuration by measuring the cooling power at the sample stage using a heater mounted to the sample socket and monitor the temperature with a ruthenium-oxide temperature sensor also mounted to the sample socket at zero applied magnetic field.

The resulting cooling power is shown as a function of sample socket temperature and mixing chamber temperature in Fig. 7a. The cooling power available at the sample
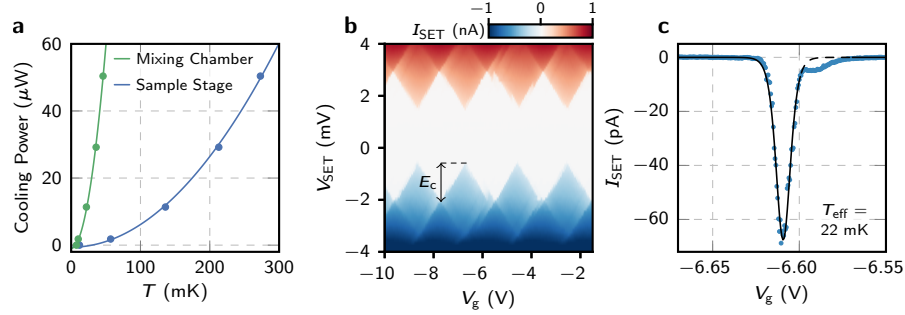
Fig. 7 **a** Cooling power as a function of temperature measured at the sample stage (depicted in Fig. 1b) and at the mixing chamber. Solid curves are quadratic fits to the data. **b** I_{SET} as a function of V_{SET} and V_g showing Coulomb diamonds at base temperature. E_c denotes the charging energy of the SET. **c** Line cut of I_{SET} as a function of V_g through the apex of one diamond at $V_{SET} = -0.6$ mV (dashed line in **b**). A best fit (solid curve) to the data using Eq. 6 yields an effective electron temperature of 22 mK.

is substantially reduced, about 6 μW at 100 mK, but as we will show below, this is still sufficient for operation of the microscope.

Heating due to the motion of the scanner is primarily due to dielectric loss in the piezoelectric actuator. We observe that for a 30 min long raster scan covering 5 μm $\times$ 5 μm with 50 nm resolution, the temperature of the sample stage saturates at about 30 mK. If a lower temperature is desired, a smaller scan range or a slower scan rate can be used as the power dissipated by the piezoelectric actuator scales approximately linearly with the scanning frequency and quadratically with the scan range [28]. The cooling power available at the sample socket could likely be increased by annealing the copper braid or improving the thermal interface resistance of the clamped connections, for instance by using a gold plated braid or e-beam welding the braid directly to the socket and the other end to a lug for attaching to the puck body.

The coarse stepping positioners are not operating while acquiring scanning data, but they do additionally dissipate power into the puck while being used to navigate around the sample. For example, we observe that 60 steps at 100 Hz, moving the sample by $\sim$20 μm, heats the sample stage up to $\sim$120 mK and it cools back down to base temperature with a time constant of $\sim$5 min.

At these low temperatures, it can be challenging to sufficiently cool a sample or probe that must remain electrically isolated from the remainder of the cryostat, e.g. to enable electronic transport measurements. In such cases, since the thermal resistance between the phonons and the electrons typically increases rapidly with decreasing temperature, most of the cooling has to come from the measurement leads. This therefore necessitates that all the measurement leads are well thermalized so they provide effective cooling. For our cryostat, all the DC wiring looms are thermally anchored between copper plates at every stage of the DR. It is also important to prevent the measurement leads from guiding high-frequency radiation to the sample and probe which can lead to heating that raises the effective electron temperature.

To achieve this, we integrated two different electrical filtering stages into the wiring of the DR: room-temperature radio frequency (RF) π-filters, and cryogenic RC low-pass filters. The room temperature filter uses bolt-in style filter plates, model 52-970-206-TB0 from Spectrum Control (formerly APITech), mounted in a diecast box directly on the top of the cryostat with a short segment of shielded cable to extend the Faraday cage of the cryostat. This filter regulates external RF noise from entering the cryostat, with a nominal 3 dB cut-off frequency of 0.65 MHz. The cryogenic filter addresses noise originating from inside the refrigerator (e.g., triboelectric noise) and noise below the cut-off frequency of the room temperature filter. We use a printed circuit board (PCB) based design similar to [29], but tailored to the space available on the mixing chamber of our DR, to filter out noise directly before the sample puck. Mounting this filter on the mixing chamber minimizes any additional thermal noise from the RC filter. The filter comprises a copper box clamping the PCB for heat sinking, and forms separate Faraday shields around three successive filtering stages. The first stage uses a T-filter, model LFCN-225D+ from Mini-Circuits, which has a cut-off frequency of 350 MHz, then there are two successive RC filter stages with a combined cut-off frequency of 86 kHz.

To characterize the effectiveness of the filtering, we use Coulomb blockade thermometry to measure the electron temperature of a scanning SET tip [27]. Figure 7b shows the SET current measurement as a function of V_g and SET source-drain bias V_SET while the DR is at base temperature. Sharp Coulomb blockade diamonds are clearly resolved when the SET is biased above the superconducting gap. The charging energy E_c of the SET can be extracted from the depth of the Coulomb blockade diamonds (arrow in Fig. 7b). When the SET is biased marginally above the superconducting critical bias, the Coulomb blockade oscillations appear as sharp peaks in the SET current as a function of V_g, see Fig. 7c. The width of this peak is temperature limited when the tunneling conductance is sufficiently small such that the tunneling rate Γ is small compared with the temperature, $\hbar\Gamma \ll k_\mathrm{B}T$. In the metallic regime, where many energy levels of the island are excited by thermal fluctuations, the line shape of an individual current peak is given by [27]

$$\frac{|I_\mathrm{SET}(V_\mathrm{g})|}{|I_\mathrm{SET}|_\mathrm{max}} \approx \cosh^{-2}\left(\frac{e\alpha\Delta V}{2.5k_\mathrm{B}T}\right), \tag{6}$$

where $\Delta V = V_\mathrm{g} - V_0$ is the gate voltage difference to the center of the conductance peak V_0, and α characterises the ratio of the gate capacitance to the island's self capacitance which can be extracted from the aspect ratio of the Coulomb diamonds.

In Fig. 7c, we fit the measured SET current peak to Eq. 6, from which we obtain an effective electron temperature of $T_\mathrm{eff} = 22$ mK. We note that the shoulder in Fig. 7c is an artifact of the tip, likely related to unstable charges in or near the island. Fitting to other current peaks also yields a similar electron temperature: <30 mK (see Supplementary Information). For comparison, before the addition of the filters, the measured effective electron temperature was $T_\mathrm{eff} = 120$ mK. With the filters the extracted electron temperature is close to the reading of the calibrated temperature sensor on the sample stage, 13 mK during these measurements, indicating the filters are efficiently thermalizing the electrons on the tip.

17
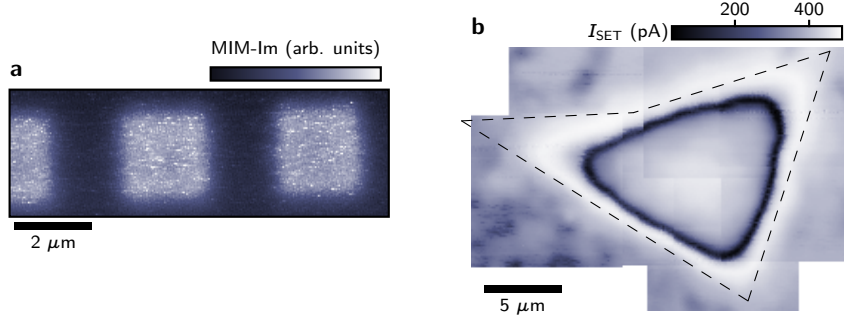
Fig. 8 **a** Constant height MIM-Im scan of a 2 μm $\times$ 2 μm gold dot pattern with a 4 μm period. **b** Spatial map of $I_{\mathrm{SET}}(x, y)$ in the vicinity of a patterned triangular hole feature in a gold film. The image corresponds to multiple scans stitched together, all taken at constant height $\lesssim 1$ μm above the test sample, and at fixed $V_{\mathrm{g}} = 1.2$ V. The black dashed line marks the physical boundary of the patterned feature.

5 Imaging and scanner calibration

Finally, we demonstrate the imaging capability using both MIM and SET modalities in the dry DR. In Fig. 8a we show an MIM-Im image taken at a fixed height of $\sim$100 nm above a calibration sample consisting of a 2 μm $\times$ 2 μm dot pattern with a 4 μm period, patterned in a 20 nm thick gold film on a Si/SiO$_2$ substrate. This sample serves as a calibration of the piezoelectric scanner range, and was used to quantify the relative in-plane tip-sample vibrations determined in Sec. 3.2. We also demonstrate SET imaging of a pre-patterned triangular hole in the gold film sample described previously: maintaining a constant tip height of $\lesssim 1$ μm above the sample and fixed $V_{\mathrm{g}} = 1.2$ V, scanning in the xy plane yields the spatial map of I_{SET} shown in Fig. 8b. This map is constructed by stitching together several adjacent scan frames taken with identical parameters, demonstrating the stability of the SET response, and the corresponding I_{SET} modulations match well to the shape of the patterned triangular hole (dashed outline in Fig. 8b).

6 Outlook

In summary, we describe the construction of two minimally-customized DR scanning systems, provide a systematic study of their vibrational performance, obtain an effective electron temperature of $<$30 mK in the scanning probe, and demonstrate the scanning capability of two different probes.

The main factory installed vibration isolation measures that limit the mechanical coupling between the pulse tube and the cryostat are the remote motor operation of the pulse tube, flexible copper braids for the thermal connection at the cold ends of the pulse tube, and a rubber vibration damping mount with a flexible vacuum bellows for the room temperature seal. The resultant absolute RMS vibration level in the bottom loading sample puck is $<$200 nm in the vertical direction, integrated up to 1 kHz, and a few microns in the horizontal directions. Notably, the total vibration

18

level is dominated by structural modes of the cryostat that are close in frequency to a harmonic of the pulse tube frequency.

Rigidly mounting the SPM in the puck achieves a relative tip-sample vibration level of 30 nm in the z direction, integrated up to 1 kHz, and $\sim$150 nm in the x and y directions. These vibration levels are sufficiently low for certain scanning applications, setting a lower limit for the tip-sample working distance of $\sim$100 nm and a spatial resolution of several hundred nanometers. In this configuration the microscope is suitable for studying bulk or thin film samples where the length scales of interest are on the sub-micron scale, while at ultra-low temperatures, in high magnetic field, and with multiple types of scanning probes. Quantum anomalous Hall thin film samples could serve as an immediate candidate, with the capability of measuring current distributions and local conductivity from different conduction channels in the bulk and at the edge [30–33].

Our data also help identify possible schemes to further reduce the vibration levels. The absolute vibrations of the sample puck are mostly below 20 Hz, the largest of which directly couple to the relative tip-sample vibrations. However, the remainder of the dominant tip-sample vibrations are at higher frequencies. The main microscope body, which currently is the standard bottom loading sample puck, could be significantly stiffened by replacing the four support rods that hold the probe and nanopositioners with a structure that has a higher bending stiffness, such as a section of a cylindrical tube [13]. If instead, the limitation of the microscope stiffness is the nanopositioners, a spring based damping could be incorporated into the sample puck, suspending a secondary structure for the microscope body. The resonance frequency of a mass-on-spring, depends only on the extension length of the spring. The puck is not tall enough to accommodate a very low cut-off frequency spring, but a cut-off below 10 Hz should still be possible which should provide significant damping at higher frequencies.

As well as stiffening and better isolating the microscope, additional modifications could be implemented to the DR to reduce the absolute vibration level at the sample puck. It has been demonstrated that isolating the remote motor assembly of the pulse tube from the cryostat in a way that allows the motor assembly to swing as the high pressure lines expand and contract, rather than pushing on the DR, can further reduce vibrations [12]. The structural modes of the fridge identified with the geophone measurements could also be modified, for instance by adding additional bracing to the DR, to move them away from harmonics of the pulse tube frequency. Another possible solution using a helium 'battery' has been demonstrated for scanning SQUID microscopy [34], which allows the pulse tube cooler to be turned off for a short period of time and the temporary cooling is provided by a large pumped volume of liquid helium. However, with such a system, measurements are not necessarily as efficient as the typical cycle time is 8–10 hours, and the DR can only run without the pulse tube for a couple of hours. An alternative to the helium 'battery', using a 1 K ^{4}He cooling circuit with better thermal isolation than the battery, has been shown to extend the hold time and may serve as an alternative for intermittent shutoff type measurements [35].

With further improvements in vibration level, we anticipate the spatial resolution of the microscope will be concurrently enhanced. This will enable the study of mesoscopic

devices and delicate nanostructures, such as van der Waals heterostructures, with spatial resolution limited by the probe, rather than vibration.

Supplementary Information. This article has an accompanying supplementary information file.

Declarations

Conflict of interest. Z.-X.S. is a co-founder of PrimeNano Inc., which licensed the microwave impedance microscopy technology from Stanford University for commercial instruments. The remaining authors declare no competing interests.

Ethics approval. The submitted work is original and has not been published elsewhere in any form or language (partially or in full).

Consent to participate. All authors consent to participate.

Consent to publication. All authors consent to publication.

Data availability. The data are available from the corresponding authors upon reasonable request.

Code availability. The code that support these findings are available from the corresponding authors upon reasonable request.

Author contributions. M.E.B., J.Y., and Y.L. helped design and install the DR and microscope at SLAC, and J.G. and G.R.A. led design and installation at UIUC. M.E.B., Z. Jiang, and J.G. conducted the geophone measurements. Y.L., J.Y., M.E.B., and Y.H. conducted the scanning SET measurements. M.E.B. conducted the MIM measurements. M.E.B. and Y.L. designed and tested the filtering. Y.L. and J.C.H. designed and fabricated test samples. B.E.F., A.K., Z.-X.S., K.A.M., D.J.V.H. supervised the work. All authors contributed to the writing of the manuscript.

References

[1] Das, P., de Ouboter, R.B., Taconis, K.W.: A Realization of a London-Clarke-Mendoza Type Refrigerator. In: Daunt, J.G., Edwards, D.O., Milford, F.J., Yaqub, M. (eds.) Low Temperature Physics LT9, pp. 1253–1255. Springer, Boston, MA (1965). https://doi.org/10.1007/978-1-4899-6443-4_133

[2] Zu, H., Dai, W., de Waele, A.T.A.M.: Development of dilution refrigerators— A review. Cryogenics **121**, 103390 (2022) https://doi.org/10.1016/j.cryogenics. 2021.103390

[3] Tomaru, T., Suzuki, T., Haruyama, T., Shintomi, T., Yamamoto, A., Koyama, T., Li, R.: Vibration analysis of cryocoolers. Cryogenics **44**(5), 309–317 (2004) https://doi.org/10.1016/j.cryogenics.2004.02.003

[4] Chijioke, A., Lawall, J.: Vibration spectrum of a pulse-tube cryostat from 1Hz to 20kHz. Cryogenics **50**(4), 266–270 (2010) https://doi.org/10.1016/j.cryogenics. 2010.01.005

[5] Olivieri, E., Billard, J., De Jesus, M., Juillard, A., Leder, A.: Vibrations on pulse tube based Dry Dilution Refrigerators for low noise measurements. Nucl. Instrum. Methods Phys. Res. A **858**, 73–79 (2017) https://doi.org/10.1016/j.nima.2017. 03.045

[6] D'Addabbo, A., Bucci, C., Canonica, L., Di Domizio, S., Gorla, P., Marini, L., Nucciotti, A., Nutini, I., Rusconi, C., Welliver, B.: An active noise cancellation technique for the CUORE Pulse Tube cryocoolers. Cryogenics **93**, 56–65 (2018) https://doi.org/10.1016/j.cryogenics.2018.05.001

[7] Song, Y.J., Otte, A.F., Shvarts, V., Zhao, Z., Kuk, Y., Blankenship, S.R., Band, A., Hess, F.M., Stroscio, J.A.: Invited Review Article: A 10 mK scanning probe microscopy facility. Rev. Sci. Instrum. **81**(12), 121101 (2010) https://doi.org/10. 1063/1.3520482

[8] Hudson, E.W., Simmonds, R.W., Yi Leon, C.A., Pan, S.H., Davis, J.C.: A very low temperature vibration isolation system. Czech. J. Phys. **46**(5), 2737–2738 (1996) https://doi.org/10.1007/BF02570355

[9] de Wit, M., Welker, G., Heeck, K., Buters, F.M., Eerkens, H.J., Koning, G., van der Meer, H., Bouwmeester, D., Oosterkamp, T.H.: Vibration isolation with high thermal conductance for a cryogen-free dilution refrigerator. Rev. Sci. Instrum. **90**(1), 015112 (2019) https://doi.org/10.1063/1.5066618

[10] Pelliccione, M., Sciambi, A., Bartel, J., Keller, A.J., Goldhaber-Gordon, D.: Design of a scanning gate microscope for mesoscopic electron systems in a cryogen-free dilution refrigerator. Rev. Sci. Instrum. **84**(3), 033703 (2013) https: //doi.org/10.1063/1.4794767

[11] Geaney, S., Cox, D., Hönigl-Decrinis, T., Shaikhaidarov, R., Kubatkin, S.E., Lindström, T., Danilov, A.V., de Graaf, S.E.: Near-Field Scanning Microwave Microscopy in the Single Photon Regime. Sci. Rep. **9**(1), 12539 (2019) https: //doi.org/10.1038/s41598-019-48780-3

[12] den Haan, A.M.J., Wijts, G.H.C.J., Galli, F., Usenko, O., van Baarle, G.J.C.,

van der Zalm, D.J., Oosterkamp, T.H.: Atomic resolution scanning tunneling microscopy in a cryogen free dilution refrigerator at 15 mK. Rev. Sci. Instrum. **85**(3), 035112 (2014) https://doi.org/10.1063/1.4868684

[13] Low, D., Ferguson, G.M., Jarjour, A., Schaefer, B.T., Bachmann, M.D., Moll, P.J.W., Nowack, K.C.: Scanning SQUID microscopy in a cryogen-free dilution refrigerator. Rev. Sci. Instrum. **92**(8), 083704 (2021) https://doi.org/10.1063/5.0047652

[14] Scheidegger, P.J., Diesch, S., Palm, M.L., Degen, C.L.: Scanning nitrogen-vacancy magnetometry down to 350 mK. Appl. Phys. Lett. **120**(22), 224001 (2022) https://doi.org/10.1063/5.0093548

[15] Zhou, H., Auerbach, N., Roy, I., Bocarsly, M., Huber, M.E., Barick, B., Pariari, A., Hücker, M., Lim, Z.S., Ariando, A., Berdyugin, A.I., Xin, N., Rappaport, M., Myasoedov, Y., Zeldov, E.: Scanning SQUID-on-tip microscope in a top-loading cryogen-free dilution refrigerator. Rev. Sci. Instrum. **94**(5), 053706 (2023) https://doi.org/10.1063/5.0142073

[16] Cao, L.W., Wu, C., Bhattacharyya, R., Zhang, R., Allen, M.T.: MilliKelvin microwave impedance microscopy in a dry dilution refrigerator. Rev. Sci. Instrum. **94**(9), 093705 (2023) https://doi.org/10.1063/5.0159548

[17] Schiessl, D., Kirtley, J.R., Paulius, L., Rosenberg, A.J., Palmstrom, J.C., Ullah, R.R., Holland, C.M., Fung, Y.-K.-K., Ketchen, M.B., Gibson, Jr., G.W., Moler, K.A.: Determining the vibrations between sensor and sample in SQUID microscopy. Appl. Phys. Lett. **109**(23), 232601 (2016) https://doi.org/10.1063/1.4971201

[18] Shperber, Y., Vardi, N., Persky, E., Wissberg, S., Huber, M.E., Kalisky, B.: Scanning SQUID microscopy in a cryogen-free cooler. Rev. Sci. Instrum. **90**(5), 053702 (2019) https://doi.org/10.1063/1.5087060

[19] Bishop-Van Horn, L., Cui, Z., Kirtley, J.R., Moler, K.A.: Cryogen-free variable temperature scanning SQUID microscope. Rev. Sci. Instrum. **90**(6), 063705 (2019) https://doi.org/10.1063/1.5085008

[20] Batey, G., Chappell, S., Cuthbert, M.N., Erfani, M., Matthews, A.J., Teleberg, G.: A rapid sample-exchange mechanism for cryogen-free dilution refrigerators compatible with multiple high-frequency signal connections. Cryogenics **60**, 24–32 (2014) https://doi.org/10.1016/j.cryogenics.2014.01.007

[21] van Kann, F., Winterflood, J.: Simple method for absolute calibration of geophones, seismometers, and other inertial vibration sensors. Rev. Sci. Instrum. **76**(3), 034501 (2005) https://doi.org/10.1063/1.1867432

[22] Chu, Z., Zheng, L., Lai, K.: Microwave Microscopy and Its Applications.

Annu. Rev. Mater. Res. **50**(1), 105–130 (2020) https://doi.org/10.1146/annurev-matsci-081519-011844

[23] Barber, M.E., Ma, E.Y., Shen, Z.-X.: Microwave impedance microscopy and its application to quantum materials. Nat. Rev. Phys. **4**(1), 61–74 (2022) https://doi.org/10.1038/s42254-021-00386-3

[24] Cui, Y.-T., Ma, E.Y., Shen, Z.-X.: Quartz tuning fork based microwave impedance microscopy. Rev. Sci. Instrum. **87**(6), 063711 (2016) https://doi.org/10.1063/1.4954156

[25] Yoo, M.J., Fulton, T.A., Hess, H.F., Willett, R.L., Dunkleberger, L.N., Chichester, R.J., Pfeiffer, L.N., West, K.W.: Scanning Single-Electron Transistor Microscopy: Imaging Individual Charges. Science **276**(5312), 579–582 (1997) https://doi.org/10.1126/science.276.5312.579

[26] Yu, J., Foutty, B.A., Han, Z., Barber, M.E., Schattner, Y., Watanabe, K., Taniguchi, T., Phillips, P., Shen, Z.-X., Kivelson, S.A., Feldman, B.E.: Correlated Hofstadter spectrum and flavour phase diagram in magic-angle twisted bilayer graphene. Nat. Phys. **18**(7), 825–831 (2022) https://doi.org/10.1038/s41567-022-01589-w

[27] Kouwenhoven, L.P., Marcus, C.M., McEuen, P.L., Tarucha, S., Westervelt, R.M., Wingreen, N.S.: Electron Transport in Quantum Dots. In: Sohn, L.L., Kouwenhoven, L.P., Schön, G. (eds.) Mesoscopic Electron Transport, pp. 105–214. Springer, Dordrecht (1997). https://doi.org/10.1007/978-94-015-8839-3_4

[28] PI Ceramic GmbH, Lindenstraße, 07589 Lederhose, Germany

[29] Kuemmeth, F., Marcus, C.M.: Reducing Noise and Temperature During Measurements in Cryostats. US 9826622B2, 2017

[30] Ella, L., Rozen, A., Birkbeck, J., Ben-Shalom, M., Perello, D., Zultak, J., Taniguchi, T., Watanabe, K., Geim, A.K., Ilani, S., Sulpizio, J.A.: Simultaneous voltage and current density imaging of flowing electrons in two dimensions. Nat. Nanotechnol. **14**(5), 480–487 (2019) https://doi.org/10.1038/s41565-019-0398-x

[31] Allen, M., Cui, Y., Ma, E.Y., Mogi, M., Kawamura, M., Fulga, I.C., Goldhaber-Gordon, D., Tokura, Y., Shen, Z.-X.: Visualization of an axion insulating state at the transition between 2 chiral quantum anomalous Hall states. Proc. Natl. Acad. Sci. **116**(29), 14511–14515 (2019) https://doi.org/10.1073/pnas.1818255116

[32] Rodenbach, L.K., Rosen, I.T., Fox, E.J., Zhang, P., Pan, L., Wang, K.L., Kastner, M.A., Goldhaber-Gordon, D.: Bulk dissipation in the quantum anomalous Hall effect. APL Mater. **9**(8), 081116 (2021) https://doi.org/10.1063/5.0056796

[33] Ferguson, G.M., Xiao, R., Richardella, A.R., Low, D., Samarth, N., Nowack,

K.C.: Direct visualization of electronic transport in a quantum anomalous Hall insulator. Nat. Mater. **22**(9), 1100–1105 (2023) https://doi.org/10.1038/s41563-023-01622-0

[34] Franklin, J., Bedard, J., Sochnikov, I.: Versatile Millikelvin Hybrid Cooling Platform for Superconductivity Research. IEEE Trans. Appl. Supercond. **33**(5), 1–3 (2023) https://doi.org/10.1109/TASC.2023.3239581

[35] Uhlig, K.: Dry dilution refrigerator with pulse tube shutoff option. Cryogenics **130**, 103649 (2023) https://doi.org/10.1016/j.cryogenics.2023.103649